International Communications in Heat and Mass Transfer 158 (2024) 107896

Contents lists available at ScienceDirect

International Communications in Heat and Mass Transfer

journal homepage: www.elsevier.com/locate/ichmt

Developing a stable microchannel flow boiling heat sink with a venting membrane

Yifan Zhang [a], Wenhao Fan [a], Zikang Zhang [a], Ji Li [a,b,*], Tianyou Zhai [b], Wei Liu [a], Zhichun Liu [a,*]

[a] School of Energy and Power Engineering, Huazhong University of Science and Technology, Wuhan 430074, China
[b] State Key Laboratory of Materials Processing and Die and Mould Technology, School of Materials Science and Engineering, Huazhong University of Science and Technology, Wuhan, 430074, China

ARTICLE INFO

Keywords:
Thermal management
Flow boiling
Microchannel
Membrane distillation
Flow instability

ABSTRACT

Microchannel flow boiling can dissipate high heat fluxes, but it may face issues such as excessive pressure drops and flow instability due to the rapid bubble expansion in microchannels. In this study, we developed two types of membrane-venting heat sinks featuring either open microchannels (MV-OMC) or closed microchannels (MV-CMC). Experiment revealed that MV-OMC not only effectively reduced pressure drop but also mitigated flow instability contrasted with MV-CMC. Additionally, the impact of system pressure, inlet temperature, and flow rate on MV-OMC's performance had been discussed in detail. Reducing system pressure enhanced boiling heat transfer but aggravated pressure drop and flow instability. Moreover, increasing the inlet temperature significantly suppressed flow instability at high heat flux. At an inlet temperature of 50 °C and a flow rate of 947.9 kg/(m^2·s), the MV-OMC heat sink in negative pressure operating status stably dissipated a heat flux of 488.6 W/cm^2 with small fluctuations of ± 0.2 °C in solid temperature and ± 0.2 kPa in pressure drop. In all, this investigation revealed the potential of membrane-venting microchannel heat sinks in high heat flux scenarios where stable dissipation was required.

1. Introduction

In fields such as new energy, nuclear power, radar, and laser, the demand for heat dissipation flux is growing rapidly [1,2]. For example, the cooling requirement of insulated gate bipolar transistor (IGBT) modules has already surpassed 100 W/cm^2 and is projected to reach >500 W/cm^2 [3], which is hard to dissipate by air cooling. Therefore, it is particularly crucial to develop efficient cooling technologies based on liquid convection or phase change, such as microchannels [4,5], jet impingement [6], thin liquid film evaporation [7,8], pool boiling [9], sprays [10], and heat pipes [11], etc. Among these, microchannel flow boiling has the merits of good compactness, long heat transfer distance, high heat transfer coefficient (HTC) and large critical heat flux (CHF), thus garnering long-term attention from researchers [12].

The primary challenges faced by microchannel flow boiling under high heat flux are the elevated pressure drop, reduced heat transfer, and strong flow instability, which are related to the generation of vapor phase within the channels [13,14]. The intense phase change causes high vapor quality and flow velocity, leading to elevated frictional pressure drops and increased power consumption of flow boiling [15,16]. Issues such as bubble expansion blockages, inter-channel bubble interactions, and interactions with upstream volumes contribute to flow instability and reduced heat transfer efficiency, potentially leading to mechanical failures [17].

To improve the performance of microchannel flow boiling, researchers have conducted extensive work on flow structure [18,19], surface treatment [20], and new materials [21], etc. Strategies such as orifice restrictions to prevent vapor backflow [22], open microchannel designs facilitating bubble growth space [23], and special fin shapes to reduce flow oscillations [24,25] have been proposed and achieved better flow stability. Furthermore, surface treatments like nanowire structures [20] and porous coatings [26] have shown significant enhancements in heat transfer coefficients (HTC) and critical heat flux (CHF) performance. Combining these various approaches can further boost the efficiency of microchannel flow boiling systems [27–29], offering promising avenues for advanced thermal management in high heat flux applications.

Additionally, employing hydrophobic porous membranes in conjunction with microchannels has emerged as a novel method to

* Corresponding authors at: School of Energy and Power Engineering, Huazhong University of Science and Technology, Wuhan 430074, China.
E-mail addresses: riki@hust.edu.cn (J. Li), zcliu@hust.edu.cn (Z. Liu).

https://doi.org/10.1016/j.icheatmasstransfer.2024.107896

Available online 10 August 2024

Nomenclature

A_c	cross-section area of the heater pillar cm^2
A_w	wetting area of microchannel surface cm^2
CHF	critical heat flux W/cm^2
C_p	specific heat of water J/(kg·°C)
h	average heat transfer coefficient $W/(m^2 \cdot K)$
HTC	heat transfer coefficient $W/(m^2 \cdot K)$
k_{Cu}	thermal conductivity of copper W/(m·K)
l	length mm
MV-CMC	membrane-venting closed microchannel
MV-OMC	membrane-venting open microchannel
NMV-OMC	non-membrane-venting open microchannel
P	pressure kPa
PET	polyethylene terephthalate
PTFE	polytetrafluoroethylene
Q_{eff}	effective heat power to the heat sink W
Q'_{eff}	effective heat absorbed by fluid W
$Q_{electric}$	electric heating power W
q_{eff}	effective heat flux to the heat sink W/cm^2
t	time s
thk	thickness mm
T	temperature °C
$\dot{V}$	inlet flow rate mL/min
z	distance in z-direction mm

Greek symbols

ρ	density of liquid water kg/m^3

Subscripts

in	inlet
neg	negative pressure
nor	normal pressure
out1	original outlet of the microchannel heat sink
out2	extra outlet for venting vapor
res	reservoir
wall	microchannel wall

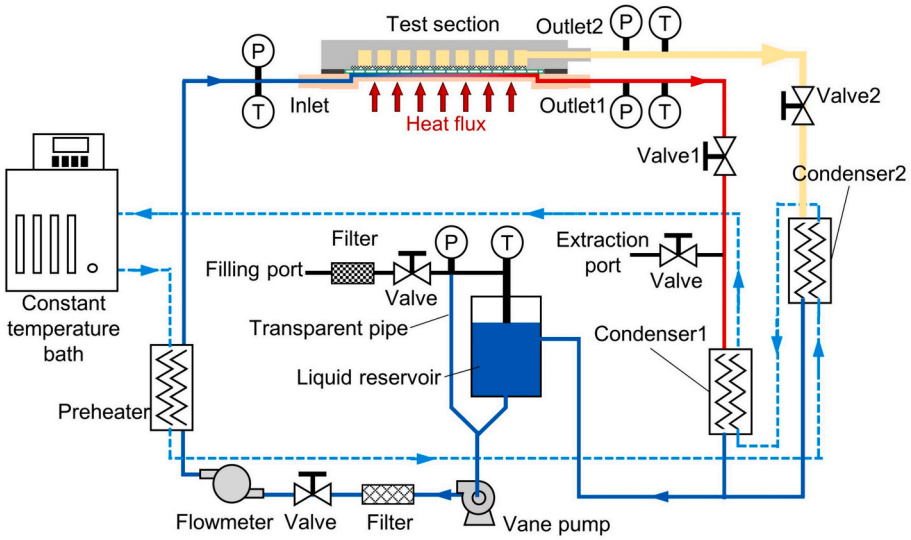

Fig. 1. Schematic diagram of the test rig. The solid blue, red, and yellow lines denote the low-temperature liquid pipe, high-temperature liquid pipe, and vapor pipe, respectively. The blue dashed line represents the coolant pipe linked to the constant temperature bath. (For interpretation of the references to color in this figure legend, the reader is referred to the web version of this article.)

improve flow boiling [15]. The majority of researchers placed the venting membranes above the channels, which can reduce vapor quality within the channel, lower pressure drops, and enhance heat transfer [16,30–32]. A minority of researchers deployed the venting membrane downstream of the microchannels instead of above the channels and also obtained improvements in pressure drop, instability, and heat transfer by promoting the bubble rupture at the outlet and inhibiting backflow [33]. In previous work [32] of this study, the membrane venting flow boiling experiment with membrane pore sizes of 0.22, 0.45, and 1.0 μm had been carried out, respectively, and tests found that a larger pore size benefited heat transfer and decreased pressure drop. In the case of a 1.0 μm pore size, the heat sink could operate without failure under a heat flux of 287.8 W/cm^2 while over half of the heat flux was dissipated vertically through the membrane.

In this study, to further enhance the performance of membrane venting flow boiling and realize high heat flux dissipation with good working stability, we considered the following three improvement measures: (a) introducing an open channel structure to reduce pressure drop and mitigate instability; (b) reducing cycle pressure to improve the boiling heat transfer at low wall temperatures; (c) changing the inlet temperature to improve instability. Based on the previous work [32], the experiments were conducted with the fluid of deionized water, the venting membrane pore size of 1.0 μm, and the wall material of copper. Thus, in this paper, the influence of vent or non-vent, open or closed channel structure, system pressure, inlet temperature, and flow rate on flow boiling performance were studied in detail. Finally, based on the experiment results, a membrane venting microchannel device with heat flux over 400 W/cm^2 and good operating stability was proposed.

2. Experimental setups

2.1. Test loop

Fig. 1 displays the configuration of the test rig. The loop employed

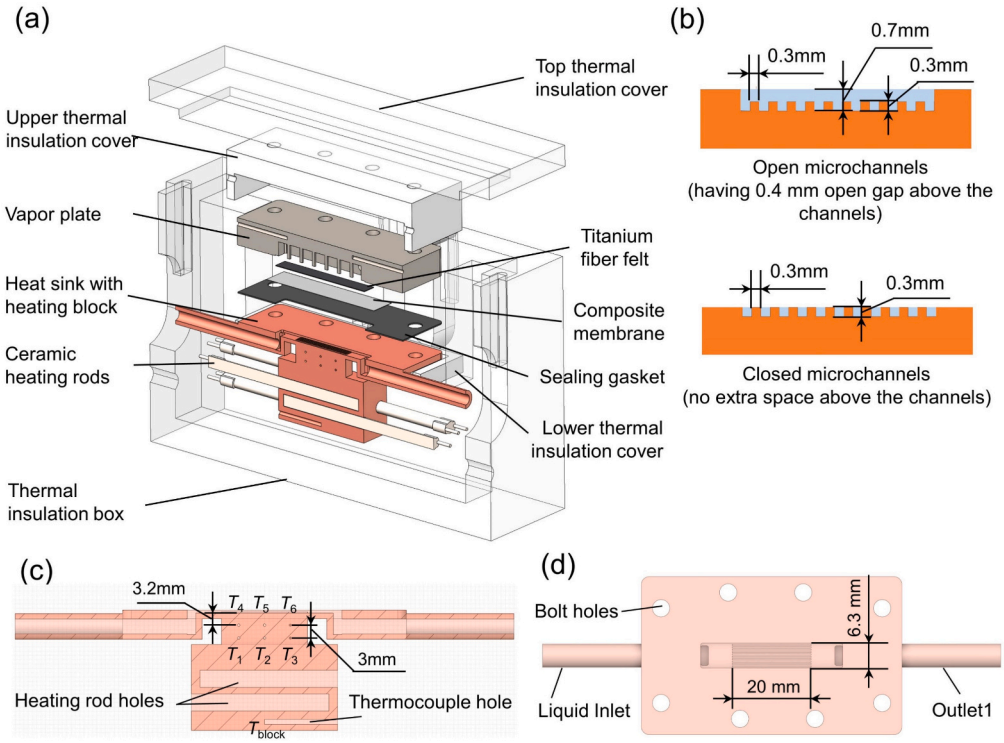

Fig. 2. Schematic diagram of the test section components: (a) Explosive view of the test section; (b) Partial sectional view of open microchannels and closed microchannels; (c) Full sectional front view of the heat sink with heating block; (d) Top view of the heat sink.

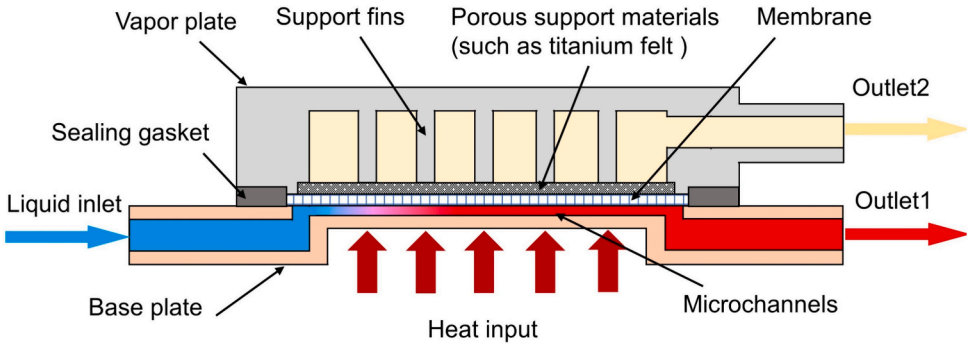

Fig. 3. Schematic of the membrane-venting microchannel heat sink.

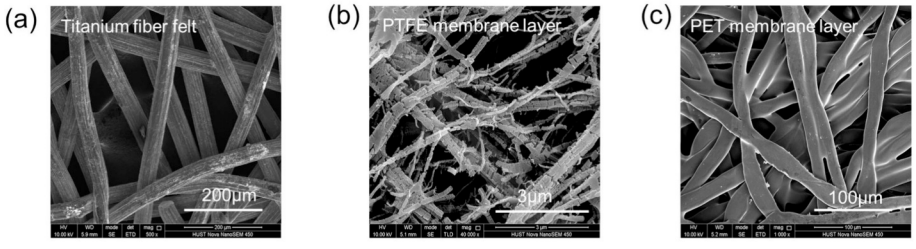

Fig. 4. SEMs of porous support material and composite membrane: (a) Titanium felt for supporting; (b) PTFE hydrophobic layer of the composite membrane; (c) PET support layer of the composite membrane.

deionized water as the working fluid and was driven by a vane pump (DC55JE-24,320) with a maximum head of 32 m and a maximum flow rate of 2.0 m^3/h. A transparent pipe was set up parallel to the reservoir to monitor the liquid level. To prevent impurities from blocking the gear meter or microchannel, a 40 μm filter was arranged upstream of the gear meter. The inlet liquid was heated to a specific temperature via a preheater (plate heat exchanger) before entering the microchannel heat sink. Two outlets, named outlet1 and outlet2, were fabricated on the heat sink to transfer liquid and vapor respectively to prevent intense gas-liquid mixing flow. At low heat flux, the heat transfer was at single-phase regime, and most fluid flowed out of the heat sink through outlet1 in liquid state. At high heat flux, the regime was flow boiling. A

Table 1
Uncertainties of parameters.

Measured parameters	Uncertainties	Calculated parameters	Uncertainties
$Q_{electric}$	±0.5%	Q_{eff}	±20 W
T_{in}, T_{out1}, T_{out2}	±0.5 °C	Q_{eff}	±15 W
T_1-T_6	±0.5 °C	q_{eff}	±16 W/cm^2
P_{in}, P_{out1}, P_{out2}	±0.6 kPa	T_{wall}	±0.4 °C
P_{res}	±0.4 kPa	T_f^*	±1.5 °C
$\dot{V}$	±2 mL/min	ΔP	±0.9 kPa
		h	± 1800 W/(m^2·K)

* The temperature uncertainty was estimated according to the saturation temperature variation of water with the pressure.

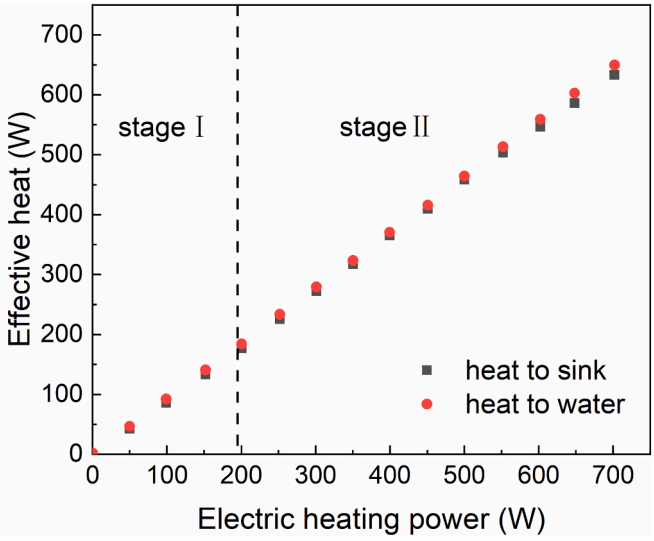

Fig. 5. Effective heat versus electric heating power of NMV-OMC heat sink in single-phase and subcooled flow boiling experiment under normal pressure, T_{in} = 20 °C and $\dot{V}$ = 200 mL/min.

portion of vapor permeated through the membrane and then flowed out of the outlet2 in vapor state, while the rest exited through outlet1 in two phase mixing state. The vapor and liquid were cooled in condensor1 and condensor2, respectively, by the coolant of a mixture of 50% ethylene glycol and 50% water from a constant temperature bath. The coolant first flowed out from the constant temperature bath, then flowed through the preheater, vapor condenser, and liquid condenser sequentially. The correspondingly physical photo of the test rig was exhibited in Supplementary Fig. 1.

The temperature and pressure measurement points included the inlet (T_{in} and P_{in}), the liquid outlet (T_{out} and P_{out}), and the vapor outlet (T_v and P_v). K-type thermocouples were used for temperature measurement. The temperature signals were collected by a digital meter (Keithley-2700) mounted with a data acquisition card. The pressure of the inlet and outlets was measured by pressure transmitters (SX-QDL80A-G). The signals from the pressure transmitters were collected and transmitted at a frequency of 10 Hz. The internal pressure of the reservoir was measured by a digital pressure gauge (SUX-YB80). Volume flow rates were obtained through a tiny elliptic gear flowmeter (CX-M5.2-SS).

2.2. Test section

Fig. 2(a) illustrates the components of the test section. The heat sink and heating block were integrated to minimize measurement errors on account of thermal contact resistance. Six ceramic heating rods were inserted into the heating block. A voltage regulator was used to regulate the electric heating power of the heating rods, and a power meter (PF9800) was utilized to measure the power. The composite membrane was bolstered by a titanium fiber felt and support fins of the vapor plate to prevent excessive deformation and mechanical damage of composite membrane. The upper vapor plate was sealed to the lower heat sink with a customized fluoroelastomer gasket. Thermal insulation covers and box were made from PTFE and employed for isolation. The heat sink, plate, and some covers were connected using eight bolts. The correspondingly actual photo of the test section was shown in Supplementary Fig. 2.

Fig. 2(c-d) depicts the heat sink featuring an effective working area with a length of 20 mm and a width of 6.3 mm. The cross-section area of the heater pillar and microchannel was also 20 mm × 6.3 mm. Furthermore, an array of thermocouple holes (T_1-T_6) was manufactured for heat flux measurement. The vertical spacing between the downside thermocouple holes of T_1, T_2, T_3 and the upper holes of T_4, T_5, T_6 was 3.0 mm, and the distance between the upper thermocouple holes and the surface of the microchannel was 3.2 mm. The microchannels and thermocouple holes were machined by high-precision CNC tools. As shown in Fig. 2(b), two types of heat sinks were machined for performance comparison. The open microchannel heat sink has a flow cross-sectional area of 3.51 mm^2, while the closed one has a smaller area of 0.99 mm^2.

Fig. 3 presents the schematic of the membrane-venting microchannel heat sink, in which a hydrophobic porous membrane is incorporated above the microchannels. The porous support material and support fins collectively provide mechanical support for the membrane. The color of the fluid is indicative of its temperature, which is influenced by the operational parameters of the system and may not precisely align with the actual temperature. As the liquid water vaporizes due to the heat flux, a portion of the vapor permeates the porous membrane, and exits through the outlet2, which means that the additional vapor path largely reduces the vapor quality within the microchannels, thereby diminishing the pressure drop of the heat sink.

2.3. Materials

The heat sink together with heating block was fabricated from copper for its exceptional thermal conductivity. The material of the vapor plate was stainless steel 304 to achieve anti-corrosion. As depicted in Fig. 4(a), the titanium fiber felt for supporting membrane has many micropores, allowing vapor permeation with little resistance. Referring to the conclusion of prior research on venting membrane heat sink [32], a two-layer composite membrane (0.16 mm thickness, LONGJIN) was adopted for its good vapor permeability. The composite membrane has a hydrophobic layer of PTFE and a support layer of PET. The hydrophobic layer interfaces with the microchannels after assembly, and the support layer interfaces with the titanium fiber felt. As shown in Fig. 4(b, c), the hydrophobic layer has a nominal pore size of 1.0 um, while the support layer has a much larger pore size. Since the water contact angle of the hydrophobic layer is 142 ± 3° (Kruss-DSA30, sessile drop method), the layer can effectively impede the infiltration of liquid water. The pore size of the membrane depends mainly on the breakthrough pressure, which varies with the test setup and operating conditions. Larger pore size may benefit the heating performance, which can be investigated in the future. In the subsequent experiments, an airtight silicone rubber membrane (0.2 mm thickness) was utilized to compare the impact of vent or non-vent.

2.4. Test process

Before conducting formal experiments, the heat measurement accuracy was validated by single-phase and subcooled flow boiling experiments. Subsequently, the flow boiling performance of membrane-venting open microchannel (MV-OMC) and non-membrane-venting open microchannel (NMV-OMC) heat sinks were compared under the conditions of porous and airtight membranes employed, respectively. In addition, the study further compared the performance of MV-OMC and

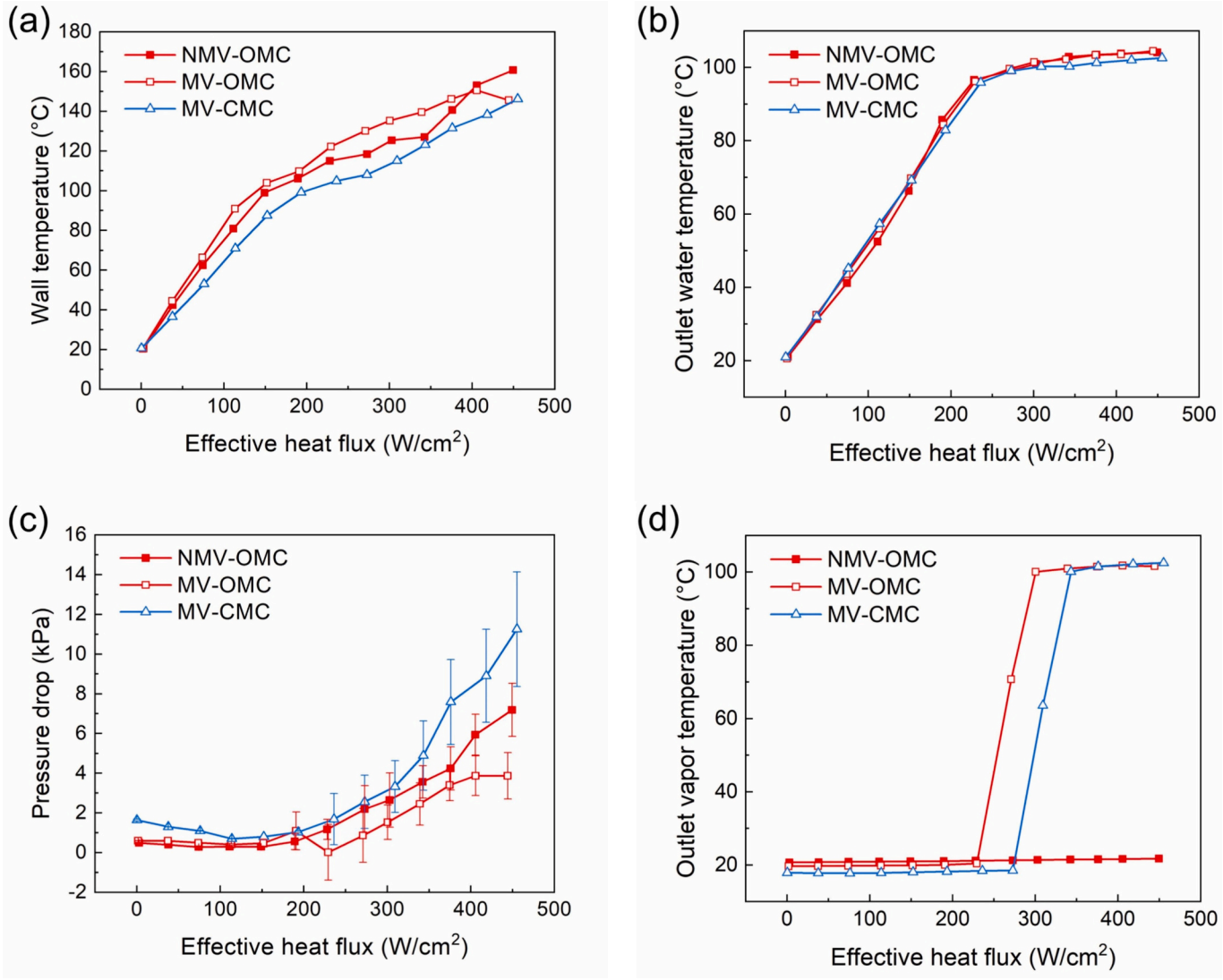

Fig. 6. Characteristics versus effective heat flux of NMV-OMC, MV-OMC, and MV-CMC heat sinks under normal pressure, an inlet temperature of 20 °C, and an inlet rate of 50 mL/min: (a) Wall temperatures; (b) Outlet water temperatures; (c) Pressure drops (error bars: standard deviation during 30s); (d) Outlet vapor temperatures.

membrane-venting closed microchannel (MV-CMC). Furthermore, the influence of system pressure, inlet temperature, and flow rate on the MV-OMC heat sink were explored in detail. Finally, for an optimal combination of parameters of the MV-OMC heat sink, we measured its performance characteristic curves.

Experiments were initiated after filling the system with deionized water. The liquid level in the reservoir was kept slightly above its center. The inlet temperature was controlled within ±1 °C of the desired temperature throughout the tests. The electric power to heating rods increased with the increment of 50 W. Each test condition was sustained for >5 min after stabilization. In consideration of the material temperature resistance (190 °C) and the safety of the experiment, the experiment would be terminated once either the temperature of the heating block in proximity to the heating rod (T_{block}) reached 300 °C or the wall temperature (T_{wall}) reached 150 °C. Consequently, the CHF was not reached during the experiments for all the configurations.

3. Data reduction

The effective heat conducted to the heat sink, Q_{eff}, was calculated as:

$$Q_{eff} = A_c q_{eff} \tag{1}$$

where A_c is the cross-section area of the heater pillar, and q_{eff} is the effective heat flux.

The effective heat flux can be calculated from the measured temperature gradient according to the Fourier's law:

$$q_{eff} = k_{Cu}\frac{\Delta T}{\Delta z} = k_{Cu}\frac{(T_1+T_2+T_3)-(T_4+T_5+T_6)}{3\Delta z} \tag{2}$$

where k_{Cu} is the thermal conductivity of copper. T_1-T_6 are the temperatures measured at the heater pillar as shown in Fig. 2(c), and Δz is the vertical distance between the downside thermocouple holes of T_1, T_2, T_3 and the upper holes of T_4, T_5, T_6.

Based on the one-dimensional heat conduction assumption, the wall temperature at the surface of microchannels, T_{wall}, can be estimated as:

$$T_{wall} = \frac{T_4+T_5+T_6}{3} - \frac{q_{eff}\Delta z'}{k_{Cu}} \tag{3}$$

where Δz' is the distance between the upper thermocouple holes of T_4, T_5, T_6 and the surface of the microchannels.

For the condition of single-phase and subcooled flow boiling, the effective heat can also be calculated from the fluid temperature rise between the outlet1 and inlet.

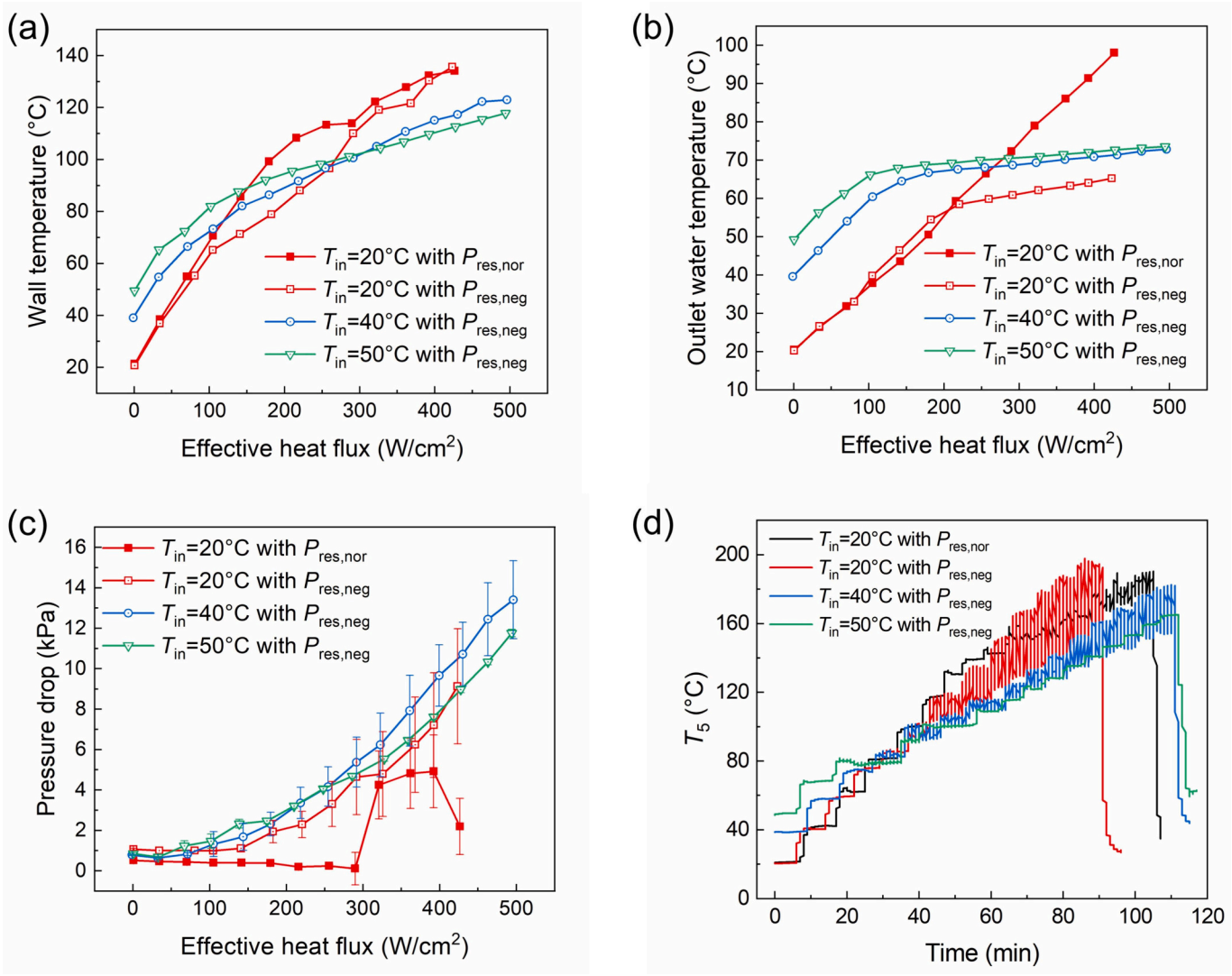

Fig. 7. Characteristics curves of the MV-OMC heat sink under normal pressure or negative pressure, and $\dot{V}$ = 100 mL/min, T_{in} = 20, 40, or 50 °C: (a) Wall temperatures versus effective heat fluxes; (b) Outlet water temperatures versus effective heat fluxes; (c) Pressure drops versus effective heat fluxes (error bars: standard deviation during 30s); (d) T_5 (a temperature of the heat block) versus time.

$$Q'_{eff} = \rho \dot{V} C_p (T_{out1} - T_{in}) \tag{4}$$

where Q'_{eff} is the effective heat absorbed by fluid. ρ, $\dot{V}$ and C_p are the density, inlet flow rate, and specific heat of liquid water, respectively.

The pressure drop of the heat sink was calculated as the pressure difference between the inlet and outlet1. The validation of the pressure measurement was shown in Supplementary Section 2.

$$\Delta P = P_{in} - P_{out1} \tag{5}$$

In addition, the HTC was calculated as:

$$h = \frac{Q_{eff}}{A_w (T_{wall} - T_f)} \tag{6}$$

where A_w is the wetting area of microchannel surface, and T_f is the fluid temperature. The A_w has a value of 1.998 cm^2 for MV-CMC and 2.758 cm^2 for MV-OMC. For single-phase and subcooled flow boiling, T_f was calculated by the average temperature of the inlet and outlet1. For saturated flow boiling, T_f was set as the saturation temperature according to the average pressure of inlet and outlet1 [34]. As the temperature and pressure fluctuations existed, the data in the text were averaged over 30 s unless otherwise specified.

The uncertainties of the calculated parameters were estimated based on the standard uncertainty analysis method [21] and are listed in Table 1.

4. Results and discussion

4.1. Accuracy verification of measured heat

In this section, the Q_{eff} (heat to sink) and Q'_{eff} (heat to water) were compared to validate the measurement accuracy of the NMV-OMC heat sink. The experiment was conducted under the condition of an inlet flow rate of 200 mL/min, during which the valve at the vapor pipe was closed. The maximum outlet temperature was around 60 °C and the maximum wall temperature was about 130 °C, so the flow was either single-phase flow (stage I, left part) or subcooled boiling flow (stage II, right part). Due to the sufficient flow rate, the outlet flow remained liquid without bubbles under high heating power near the thermocouples. The latent heat of the fluid did not significantly impact the calculation of Q'_{eff}. As illustrated in Fig. 5, the two effective heat values were close to each other, proving the reliability of heat measurements. The Q_{eff} was slightly smaller than Q'_{eff} at high heat input possibly because of the enhanced radiation and convection heat transfer paths within the

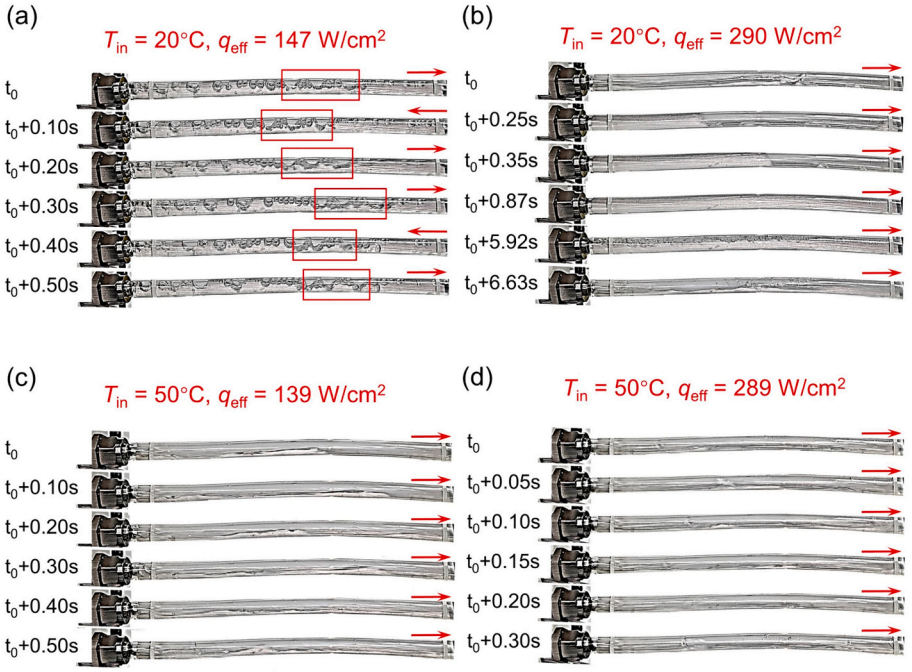

Fig. 8. Images of MV-OMC heatsink water outlet pipe under a negative pressure and a 100 mL/min inlet rate, with different inlet temperatures and heat fluxes: (a) T_{in} = 20 °C, q_{eff} = 147 W/cm^2 (b) T_{in} = 20 °C, q_{eff} = 290 W/cm^2; (c) T_{in} = 50 °C, q_{eff} = 139 W/cm^2 (d) T_{in} = 50 °C, q_{eff} = 289 W/cm^2.

thermal insulation box, which were not reflected by the temperature gradient of heater pillar. Consequently, Q_{eff} was employed to represent the effective heat in subsequent paragraphs.

4.2. Influence of membrane-vent and channel-opening

The influence of membrane-vent was tested by comparing a hydrophobic porous membrane with an airtight membrane in the heat sink of the open microchannel structure. As illustrated in Fig. 6, when the heat flux ranged from 0 to 150 W/cm^2, the wall temperature was below 100 °C and the flow was in a state of single-phase. During this range, both the wall temperature and pressure drop of the NMV-OMC were close to that of the MV-OMC. The error bars in Fig. 6(c) represented pressure fluctuations, which were very weak under the heat flux of 150 W/cm^2. As the heat flux exceeded 150 W/cm^2, the wall temperatures were above 100 °C in both NMV-OMC and MV-OMC, marking the first turning points of temperature and pressure drop curves. After further increasing the heat flux, subcooled boiling began, causing significant increments and fluctuations in pressure drops. The MV-OMC had a smaller pressure drop than NMV-OMC on account of vapor quality reduction by membrane vent [15,16,32]. Moreover, the outlet vapor temperature of the MV-OMC underwent a stepwise increase when effective heat flux surpassed 230 W/cm^2. This indicated that substantial vapor permeated the membrane. In addition, the membrane-vent had little influence on heat transfer. When the effective heat flux below 400 W/cm^2, the wall temperature in MV-OMC was close or even higher than that in NMV-OMC. Once the effective heat flux exceeded 400 W/cm^2, the wall temperature in MV-OMC was lower than that in NMV-OMC. Furthermore, this heat transfer advantage of MV-OMC was demonstrated to be repeatable under high heat flux conditions. However, the membrane-vent had a significant influence on pressure drop. The pressure drop of MV-OMC was obviously lower than that of NMV-OMC at high heat flux. These results were consistent with the previous research [32]. At a heat flux of 430 W/cm^2, the pressure drop of MV-OMC was 40% lower than that of NMV-OMC.

In addition to the impact of venting, the microchannel's open and closed structures were compared between MV-OMC and MV-CMC, as illustrated in Fig. 2(b). The flow cross-sectional area of MV-OMC was 254% larger than MV-CMC, resulting in a much lower flow velocity of MV-OMC under the same volume flow rate. Consequently, MV-CMC had lower wall temperatures and significantly higher pressure drops compared to MV-OMC, as shown in Fig. 6. Furthermore, MV-CMC had severe flow instability due to less region for bubble growth [23]. At an effective heat flux of around 400 W/cm^2, the pressure drop and pressure drop fluctuations of MV-CMC were approximately 100% higher than those of MV-OMC. In all, MV-OMC appears more suitable for dissipating high heat fluxes compared to MV-CMC. For an instance, at the same mass flux of 474 kg·m^{-2}·s^{-1} (equivalent to 100 mL/min in MV-OMC and 28.2 mL/min in MV-CMC) and the heat flux of about 300 W/cm^2, compared with MV-CMC, MV-OMC's wall temperature reduced by about 20 °C and its pressure drop reduced by over 80% (this result is not shown in a figure for avoiding repetition).

4.3. Influence of pressure and inlet temperature

The flow boiling characteristics are intricately tied to the boiling point and subcooling degree of the inlet. As illustrated in Fig. 7, the internal pressure of the test loop was decreased through the evacuation of a circulating water vacuum pump via the extraction port. The reservoir pressure of the normal pressure group ($P_{res,nor}$) was around 101 kPa, which corresponds to a boiling point of 100 °C. And reservoir pressure of the negative pressure group ($P_{res,neg}$) was approximately 20 kPa, which corresponds to a boiling point of 60 °C. Accordingly, an investigation into the impact of pressure on system performance was conducted. Fig. 7 (a) illustrates the impact of pressure on wall temperature, the $P_{res,neg}$-group had a higher heat transfer performance than the $P_{res,nor}$-group within the effective heat flux range of 100–300 W/cm^2, resulting in a significant decrease in wall temperature (around 5–20 °C). Meanwhile, the $P_{res,neg}$-group displayed higher pressure drop and pressure drop fluctuations than the $P_{res,nor}$-group, as depicted in Fig. 7(c), possibly due to the larger specific volume of vapor. There were also more noticeable temperature fluctuations in the $P_{res,neg}$-group because of more serious backflow phenomena as shown in Fig. 8(a, b). Moreover, as depicted in Fig. 7(c), a wave of pressure drop curve was observed in the $P_{res,nor}$-

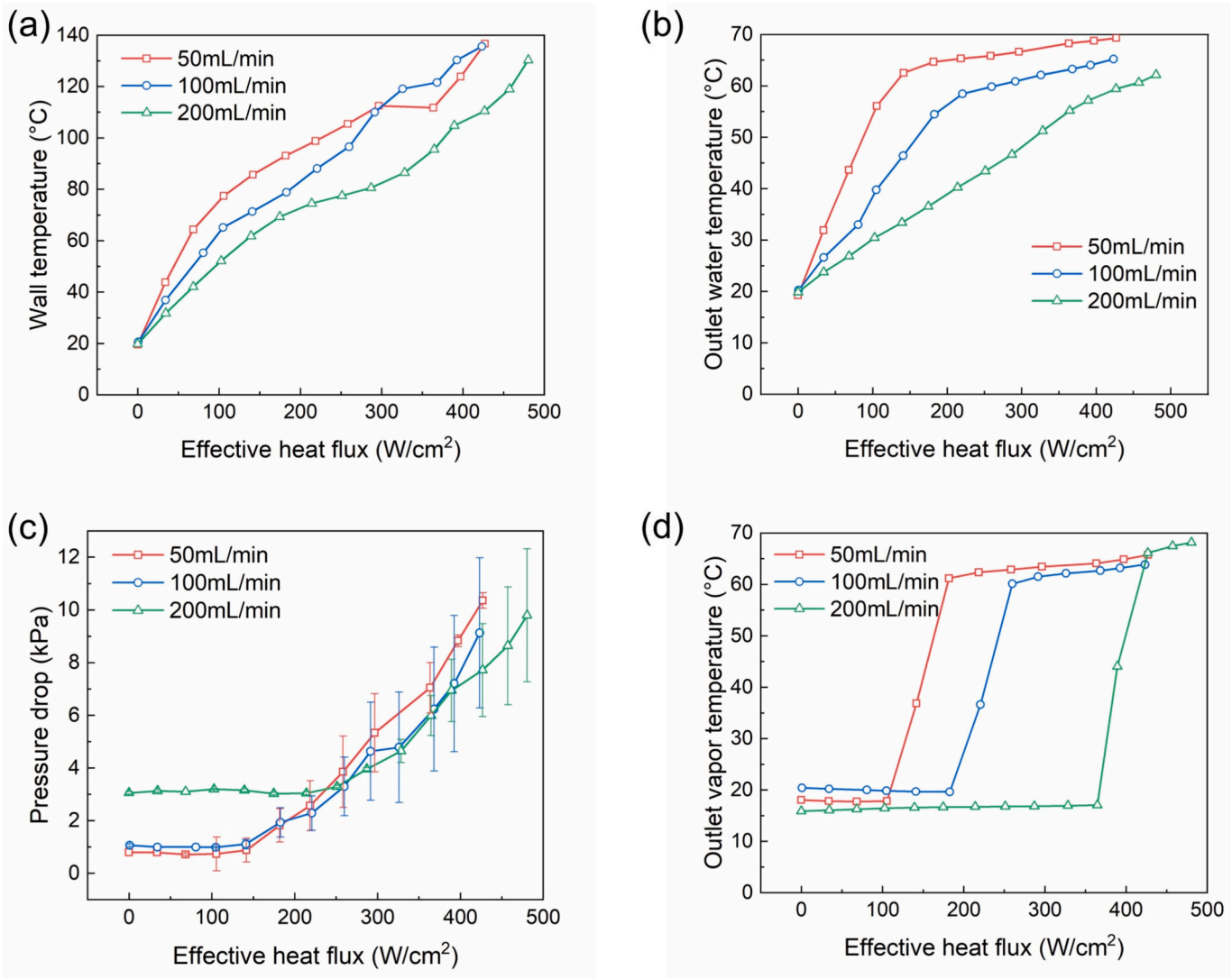

Fig. 9. Characteristics versus effective heat flux of MV-OMC heat sinks under negative pressure, $T_{in} = 50$ °C, and $\dot{V} = 50$, 100, 200 mL/min: (a) Wall temperatures; (b) Outlet water temperatures; (c) Pressure drops (error bars: standard deviation during 30s); (d) Outlet vapor temperatures.

group within the effective heat flux range of 280–430 W/cm^2. This type of curve was repeatable under identical operational conditions. The increase in pressure drop could be attributed to the fluid velocity surge during boiling. The decrease in pressure drop might be associated with the membrane-vent and flow pattern change. Besides, the pressure in microchannels increased with the heat flux, which led to an increase in the boiling point and a higher outlet water temperature, as reflected in Fig. 7(b).

As shown in Fig. 7, for the configuration of MV-OMC, negative pressure conditions with $P_{in} = 20$ kPa were also examined at various inlet temperatures ($T_{in} = 20$, 40, and 50 °C). As described in Fig. 7(b), a higher inlet temperature corresponded to an earlier turning point of outlet water temperature, because a high inlet temperature facilitated the heat transfer regime transforming from single-phase to two-phase. Notably, for a higher inlet temperature case, although the wall temperature was high at low heat flux due to a weaker single-phase heat transfer, it was low at high heat flux due to the benefit of a stable boiling flow state. At the heat flux of about 420 W/cm^2, for the $T_{in} = 20$, 40, and 50 °C, the standard deviations of pressure drop were 2.84, 1.57, and 0.15 kPa, respectively, and the standard deviation of T_5 were 16.07, 7.30, and 0.08 °C, respectively.

For $T_{in} = 20$ °C, as presented in Fig. 8(a), under conditions of subcooled boiling and a low heat flux of 147 W/cm^2, high-frequency flow oscillations were observed. The red arrow represents the direction of fluid flow in the pipe. The fluid repeatedly moved forward and backward in the heat sink, which combined with drastic temperature and pressure fluctuations as shown in Fig. 7. As presented in Fig. 8(b), with a higher heat flux of 290 W/cm^2, boiling became more intense. The outlet flow pattern appeared periodically stratified flow, single phase flow, bubble flow, etc., which indicated that the rapid bubble expansion led to a periodic shortage of liquid supply of the heat sink. Therefore, the liquid supply shortage resulted in large temperature fluctuations as exhibited in Fig. 7. When the heat flux raised further, the flow pattern didn't change a lot and was similar to that of Fig. 8(b). For $T_{in} = 50$ °C, due to a high inlet temperature, the regime would be in a saturated flow boiling with a heat flux exceeding approximately 139 W/cm^2, and the outlet flow kept stably in a stratified flow without backflow as depicted in Fig. 8(c, d). In addition, the pressure and wall temperature were also kept with no significant fluctuations. In summary, for a lower inlet temperature, the heat sink of MV-OMC could perform better at a low heat flux but worse at a high heat flux. For a higher inlet temperature, it could establish a stable flow boiling pattern and obtain much better two-phase performance at a high heat flux. However, an increased inlet temperature may not result in a reduction in pressure drop. The pressure drop is influenced by the volume flow rate, the stability of flow boiling and the distribution of gas to liquid within the channel. These factors are

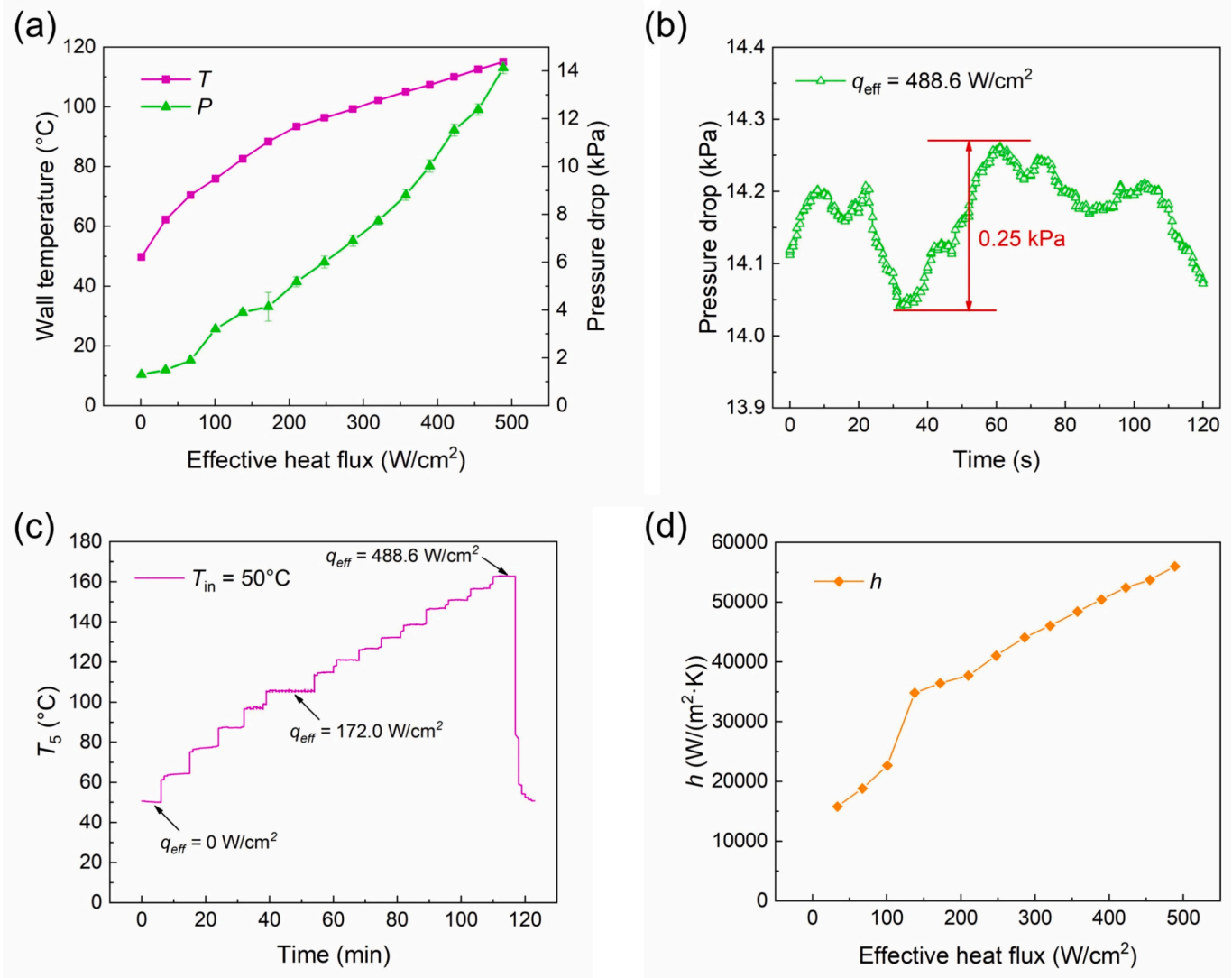

Fig. 10. Characteristics of the MV-OMC heat sink under a negative pressure, an inlet temperature of 50 °C, and an inlet rate of 200 mL/min: (a) Wall temperature and pressure drop versus effective heat flux (error bars: standard deviation during 30s); (b) Pressure drop varies in 120 s; (c) T_5 (a temperature of the heat block) changes with time; (d) Heat transfer coefficient versus effective heat flux.

inextricably linked to the inlet temperature and many other system parameters, which requires further research. Consequently, the relation between inlet temperature and heat flux of the MV-OMC heat sink shall be well considered for temperature control strategy.

4.4. Influence of inlet rate

The inlet rate is a common parameter in practical situations. As reported in Fig. 9, three different flow rates (equivalent to 237, 474, and 948 kg·m^{-2}·s^{-1}) were tested. Increasing the inlet rate resulted in reductions in wall temperatures and outlet water temperatures. Consequently, as illustrated in Fig. 9(b, d), when the inlet rate was larger, the transition from single-phase flow to subcooled boiling flow occurred at a higher heat flux. As shown in Fig. 9(c), a larger inlet rate could increase the pressure drop at low heat flux (<250 W/cm^2). However, at high heat flux (>250 W/cm^2), the pressure drops were closed to each other at different inlet rates due to the lower vapor quality of high inlet rate group. In conclusion, a higher inlet rate leads to lower wall temperatures at all heat flux and may accompany a lower pressure drop at high heat flux.

4.5. Optimal parameter combination

In view of the above-mentioned results, the optimal parameter combination was tested for the MV-OMC heat sink. Specifically, the inlet water temperature was 50 °C and the flow rate was 200 mL/min at a system pressure of 20 kPa. As seen in Fig. 10, under an effective heat flux of 488.6 W/cm^2, the MV-OMC heat sink maintained a wall temperature of 115.0 °C and a pressure drop of 14.1 kPa with small fluctuations of ± 0.2 °C in solid temperature and ± 0.2 kPa in pressure drop (standard deviation during 30s), showing that the system had good stability. In fact, except for small fluctuations existed at the transition stage from single-phase to two-phase flow (~170 W/cm^2), the heat transfer of MV-OMC was very stable at all heat flux. Additionally, as shown in Fig. 10 (d), the HTC increased with the heat flux and reached a value of ~56,000 W/(m^2·K) at an effective heat flux of 488.6 W/cm^2. However, limited by the heating power, the maximum HTC was not reached. Further increment of the HTC values will be achieved through optimization of the channel structure and improvement of the experimental setup [35]. The use of a low-boiling-point working fluid can also enhance the heat transfer performance [36]. However, the surface energy of such fluid is very low, necessitating further investigation into the development of anti-oil membranes with good mechanical and chemical

durability. In conclusion, the MV-OMC heat sink can effectively dissipate high heat flux with good stability.

5. Conclusions

This research studied the flow and heat transfer characteristics of a membrane-venting microchannel by experimental investigations. The heat sink had an effective working size of 20 × 6.3 mm^2. The experiment compared the performance differences between vent or non-vent and open or closed microchannels. Due to the good performance of MV-OMC heat sink, further investigations of MV-OMC heat sink were conducted to study the effect of system pressure, inlet temperature, and inlet rate. Finally, an optimal parameter combination was tested. The main conclusions of this study are as follows:

1. Membrane-vent enhanced heat transfer performance and flow stability of microchannel heat sink, especially at high heat flux. Notably, at a heat flux of ~430 W/cm^2, the vent group had 40% less pressure drop and its wall temperature was 20 °C lower than non-vent group.
2. The MV-OMC heat sink effectively reduced the flow resistance and instability in contrast to the MV-CMC heat sink. The pressure drop of MV-OMC heat sink was significantly reduced by approximately 70% at high heat flux (~450 W/cm^2).
3. For the MV-OMC configuration, reducing system pressure increased system pressure fluctuations. The negative pressure group had a larger pressure drop than the normal pressure group. Besides, its wall temperature was 5–20 °C lower than the normal pressure group within 100–300 W/cm^2.
4. For the MV-OMC configuration with a low system pressure, increasing inlet temperature effectively suppressed temperature and pressure fluctuations, and improved the heat transfer performance at high heat flux. In addition, increasing the inlet rate lowered the wall temperature without increasing the pressure drop at high heat flux.
5. The MV-OMC heat sink successfully dissipated a heat flux of 488.6 W/cm^2 with great operating stability at an inlet temperature of 50 °C and a flow rate of 948 kg/(m^2·s) under negative pressure, and the standard deviations of pressure drop and solid temperature were only 0.2 kPa and 0.2 °C, respectively.

Funding sources

This study is supported by the National Natural Science Foundation of China (No. 52076088).

CRediT authorship contribution statement

Yifan Zhang: Writing – original draft, Methodology, Formal analysis, Data curation. **Wenhao Fan:** Methodology. **Zikang Zhang:** Writing – original draft. **Ji Li:** Writing – review & editing, Supervision, Methodology. **Tianyou Zhai:** Methodology. **Wei Liu:** Writing – review & editing, Supervision. **Zhichun Liu:** Writing – review & editing, Supervision, Conceptualization.

Declaration of competing interest

The authors declare that they have no known competing financial interests or personal relationships that could have appeared to influence the work reported in this paper.

Data availability

Data will be made available on request.

Appendix A. Supplementary data

Supplementary data to this article can be found online at https://doi.org/10.1016/j.icheatmasstransfer.2024.107896.

References

[1] J.L. Smoyer, P.M. Norris, Brief historical perspective in thermal management and the shift toward management at the nanoscale, Heat Transf. Eng. 40 (2019) 269–282, https://doi.org/10.1080/01457632.2018.1426265.
[2] T.G. Karayiannis, M.M. Mahmoud, Flow boiling in microchannels: fundamentals and applications, Appl. Therm. Eng. 115 (2017) 1372–1397, https://doi.org/10.1016/j.applthermaleng.2016.08.063.
[3] P. Wang, P. McCluskey, A. Bar-Cohen, Two-phase liquid cooling for thermal management of IGBT power electronic module, J. Electron. Packag. Trans. ASME. 135 (2013), https://doi.org/10.1115/1.4023215.
[4] P. Cui, Z. Liu, Experimental study on flow boiling in ultrahigh-aspect-ratio copper microchannel heat sink, Appl. Therm. Eng. 223 (2023) 119975, https://doi.org/10.1016/j.applthermaleng.2023.119975.
[5] R. Kokate, C. Park, C. Mitsingas, E. Schroen, Flow boiling in parallel microchannels in a pumped two-phase loop: flow visualization and thermal characteristics, Int. Commun. Heat Mass Transf. 155 (2024) 107566, https://doi.org/10.1016/j.icheatmasstransfer.2024.107566.
[6] H.C. Cui, X.T. Lai, J.F. Wu, M.Z. Wang, W. Liu, Z.C. Liu, Overall numerical simulation and experimental study of a hybrid oblique-rib and submerged jet impingement/microchannel heat sink, Int. J. Heat Mass Transf. 167 (2021) 120839, https://doi.org/10.1016/j.ijheatmasstransfer.2020.120839.
[7] S. Narayanan, A.G. Fedorov, Y.K. Joshi, On-chip thermal management of hotspots using a perspiration nanopatch, J. Micromech. Microeng. 20 (2010) 075010, https://doi.org/10.1088/0960-1317/20/7/075010.
[8] S. Narayanan, A.G. Fedorov, Y.K. Joshi, Heat and mass transfer during evaporation of thin liquid films confined by nanoporous membranes subjected to air jet impingement, Int. J. Heat Mass Transf. 58 (2013) 300–311, https://doi.org/10.1016/j.ijheatmasstransfer.2012.11.015.
[9] N. Unno, R. Noma, K. Yuki, S.-I. Satake, K. Suzuki, Effects of surface properties on wall superheat at the onset of microbubble emission boiling, Int. J. Multiphase Flow 155 (2022) 104196, https://doi.org/10.1016/j.ijmultiphaseflow.2022.104196.
[10] R.-J. Ji, D.-Q. Zhu, X.-W. Lin, Z.-F. Zhou, B. Chen, Parametric investigation on the close-loop R410A flash spray system for high power electronics cooling under low temperature, Case Stud. Therm. Eng. 41 (2023) 102643, https://doi.org/10.1016/j.csite.2022.102643.
[11] M.A. Chernysheva, S.V. Vershinin, Y.F. Maydanik, Development and investigation of a loop heat pipe at a high concentration of heat load, Int. J. Heat Mass Transf. 197 (2022) 123316, https://doi.org/10.1016/j.ijheatmasstransfer.2022.123316.
[12] H. Sadique, Q. Murtaza, Samsher, Heat transfer augmentation in microchannel heat sink using secondary flows: a review, Int. J. Heat Mass Transf. 194 (2022) 123063, https://doi.org/10.1016/j.ijheatmasstransfer.2022.123063.
[13] W. Qu, I. Mudawar, Measurement and correlation of critical heat flux in two-phase micro-channel heat sinks, Int. J. Heat Mass Transf. 47 (2004) 2045–2059, https://doi.org/10.1016/j.ijheatmasstransfer.2003.12.006.
[14] B. Wang, Y. Hu, Y. He, N. Rodionov, J. Zhu, Dynamic instabilities of flow boiling in micro-channels: a review, Appl. Therm. Eng. 214 (2022) 118773, https://doi.org/10.1016/j.applthermaleng.2022.118773.
[15] A. Mohiuddin, R. Loganathan, S. Gedupudi, Experimental investigation of flow boiling in rectangular mini/micro-channels of different aspect ratios without and with vapour venting membrane, Appl. Therm. Eng. 168 (2020) 114837, https://doi.org/10.1016/j.applthermaleng.2019.114837.
[16] M.P. David, J. Miler, J.E. Steinbrenner, Y. Yang, M. Touzelbaev, K.E. Goodson, Hydraulic and thermal characteristics of a vapor venting two-phase microchannel heat exchanger, Int. J. Heat Mass Transf. 54 (2011) 5504–5516, https://doi.org/10.1016/j.ijheatmasstransfer.2011.07.040.
[17] Y.K. Prajapati, P. Bhandari, Flow boiling instabilities in microchannels and their promising solutions – a review, Exp. Thermal Fluid Sci. 88 (2017) 576–593, https://doi.org/10.1016/j.expthermflusci.2017.07.014.
[18] J. Lu, D. Zhuang, Y. Wang, G. Ding, Effects of vortex generator on subcooled flow boiling characteristics in micro-channel, Int. J. Heat Mass Transf. 216 (2023) 124572, https://doi.org/10.1016/j.ijheatmasstransfer.2023.124572.
[19] P. Cui, Z. Liu, H. Wu, Subcooled flow boiling in ultrahigh-aspect-ratio microchannels for high heat flux cooling, Int. Commun. Heat Mass Transf. 151 (2024) 107221, https://doi.org/10.1016/j.icheatmasstransfer.2023.107221.
[20] T. Alam, W. Li, W. Chang, F. Yang, J. Khan, C. Li, A comparative study of flow boiling HFE-7100 in silicon nanowire and plainwall microchannels, Int. J. Heat Mass Transf. 124 (2018) 829–840, https://doi.org/10.1016/j.ijheatmasstransfer.2018.04.010.
[21] Q. Yang, J. Zhao, Y. Huang, X. Zhu, W. Fu, C. Li, et al., A diamond made microchannel heat sink for high-density heat flux dissipation, Appl. Therm. Eng. 158 (2019) 113804, https://doi.org/10.1016/j.applthermaleng.2019.113804.
[22] S. Szczukiewicz, N. Borhani, J.R. Thome, Two-phase flow operational maps for multi-microchannel evaporators, Int. J. Heat. Fluid. Fl. 42 (2013) 176–189, https://doi.org/10.1016/j.ijheatfluidflow.2013.03.006.
[23] S.G. Kandlikar, T. Widger, A. Kalani, V. Mejia, Enhanced flow boiling over open microchannels with uniform and tapered gap manifolds, J. Heat Transf. 135 (2013), https://doi.org/10.1115/1.4023574.

[24] Y.K. Prajapati, M. Pathak, M.K. Khan, Bubble dynamics and flow boiling characteristics in three different microchannel configurations, Int. J. Therm. Sci. 112 (2017) 371–382, https://doi.org/10.1016/j.ijthermalsci.2016.10.021.
[25] Q. Han, Z. Liu, C. Zhang, W. Li, Enhanced single-phase and flow boiling heat transfer performance in saw-tooth copper microchannels with high L/Dh ratio, Appl. Therm. Eng. 236 (2024) 121478, https://doi.org/10.1016/j.applthermaleng.2023.121478.
[26] Z. Zhang, Y. Wu, K. He, X. Yan, Experimental investigation into flow boiling heat transfer and pressure drop in porous coated microchannels, Int. J. Heat Mass Transf. 218 (2024) 124734, https://doi.org/10.1016/j.ijheatmasstransfer.2023.124734.
[27] X. Jiang, S. Waqar Ali Shah, J. Liu, Y. Li, S. Zhang, Z. Wang, et al., Design of micro-nano structures for counter flow diverging microchannel heat sink with extraordinarily high energy efficiency, Appl. Therm. Eng. 209 (2022) 118229, https://doi.org/10.1016/j.applthermaleng.2022.118229.
[28] L. Yin, M. Sun, P. Jiang, C. Dang, L. Jia, Heat transfer coefficient and pressure drop of water flow boiling in porous open microchannels heat sink, Appl. Therm. Eng. 218 (2023) 119361, https://doi.org/10.1016/j.applthermaleng.2022.119361.
[29] Q. Zhao, D. Zhang, J. Qiu, M. Lu, J. Zhou, X. Chen, Bubble behaviors and flow boiling characteristics in open microchannels with large aspect ratio, Appl. Therm. Eng. 213 (2022) 118768, https://doi.org/10.1016/j.applthermaleng.2022.118768.
[30] A. Fazeli, S. Moghaddam, A new paradigm for understanding and enhancing the critical heat flux (CHF) limit, Sci. Rep. 7 (2017) 5184, https://doi.org/10.1038/s41598-017-05036-2.
[31] S. Li, M. Wei, Experimental study on flow boiling characteristics in continuous and segmented microchannels with vapor venting membrane, Energies 15 (2022) 8756, https://doi.org/10.3390/en15228756.
[32] J. Li, Z. Zhang, Y. Zhang, R. Zhao, H. Cui, T. Zhai, et al., High heat flux dissipation of membrane-venting heat sink with thin film boiling, Int. J. Heat Mass Transf. 221 (2024) 125078, https://doi.org/10.1016/j.ijheatmasstransfer.2023.125078.
[33] A. Priy, S. Raj, M. Pathak, M. Kaleem Khan, A hydrophobic porous substrate-based vapor venting technique for mitigating flow boiling instabilities in microchannel heat sink, Appl. Therm. Eng. 216 (2022) 119138, https://doi.org/10.1016/j.applthermaleng.2022.119138.
[34] J. Qiu, Q. Zhao, M. Lu, J. Zhou, D. Hu, H. Qin, et al., Experimental study of flow boiling heat transfer and pressure drop in stepped oblique-finned microchannel heat sink, Case Stud. Therm. Eng. 30 (2022) 101745, https://doi.org/10.1016/j.csite.2021.101745.
[35] F. Yang, X. Dai, Y. Peles, P. Cheng, J. Khan, C. Li, Flow boiling phenomena in a single annular flow regime in microchannels (I): characterization of flow boiling heat transfer, Int. J. Heat Mass Transf. 68 (2014) 703–715, https://doi.org/10.1016/j.ijheatmasstransfer.2013.09.058.
[36] V.Y.S. Lee, T.G. Karayiannis, Effect of inlet subcooling on flow boiling in microchannels, Appl. Therm. Eng. 181 (2020) 115966, https://doi.org/10.1016/j.applthermaleng.2020.115966.